Ion orbits in plasma etching of semiconductors

Tsitsi G. Madziwa-Nussinov,[a] Donald Arnush,[b] and Francis F. Chen[c]
Electrical Engineering Department, University of California, Los Angeles, California 90095-1594, USA

(Received 27 November 2006; accepted 23 October 2007; published online 9 January 2008)

Fabrication of high-speed semiconductor circuits depends on etching submicron trenches and holes with straight walls, guided by sheath accelerated ions, which strike the substrate at a normal angle. Electrons accumulate at the nonconductive entrance of each trench, charging it negatively and preventing the penetration of electrons to the bottom of the trench. This "electron shading" effect causes an ion charge at the bottom, which is well known to cause damage to thin oxide layers. In addition, the deflection of ions by electric fields in the trench can cause deformation of the trench shape. To study this effect, the ion orbits are computed self-consistently with their charging of the trench walls. It is found that (a) the orbits depend only on the electric fields at the entrance and are sensitive to changes in the shape of the photoresist layer there; (b) there is an "ion shading" effect that protects part of the wall; and (c) the number of ions striking the wall is too small to cause any deformation thereof. © *2008 American Institute of Physics*. [DOI: 10.1063/1.2819681]

I. INTRODUCTION

In plasma processing,[1–6] a planar sheath[7] separates the plasma from the silicon wafer onto which submicron circuits are built by deposition and etching. These features have a minimum size (or critical dimension CD) of 60 nm or below. The sheath thickness s is at least $5\lambda_D$, where λ_D is the Debye length defined below, and can be several times this if a large negative dc bias is applied to the wafer. If we take $n=10^{12}$ cm^{-3} and $k_BT_e=1$ eV as extreme values likely to exist at the sheath edge, we find that s is at least 37 μm, and extends over the 200–300 mm diameter of the wafer. Thus, the sheath is at least 100 times thicker than the feature sizes and orders of magnitude wider. We can therefore assume that ions emitted from the sheath edge have straight trajectories normal to the wafer as they approach its surface.

The phenomenon of electron shading[8–16] is illustrated in Fig. 1. Ions are launched from the sheath edge and are accelerated unidirectionally toward the wafer by the sheath electric field, reaching energies of tens of volts or more. Bombardment of the trench bottom loosens the first few monolayers, allowing the etchant atoms of Cl or F to combine much more effectively than without the ions. Electrons remain in an isotropic Maxwellian distribution and charge the nonconductive photoresist to its floating potential. This negative charge allows very few electrons to enter the trench; thus, the ions deposit a positive charge onto the trench bottom. If the trench is in an insulator, as in this example, no harm is done; but in the overetch period, the trench can break through into the conducting silicon layer. If this layer is connected to the gate of a transistor, this positive charge can cause a large electric field inside the gate oxide insulator, damaging it. For an oxide thickness of 20 A, say, even a 1 V potential drop across it amounts to an electric field of 5 MV/cm. This serious problem in computer chip manufacturing is well known and documented. In the present work we try to evaluate this effect quantitatively by calculating the ion orbits self-consistently with the wall charges which the ions themselves deposit.

II. SCALE INVARIANCE

If they are small enough, the exact size of the trenches is irrelevant, and a universal result can be obtained. To show this, we write Poisson's equation as

$$\varepsilon_0\hat{\nabla}^2\hat{V}=e(n_e-n_i), \tag{1}$$

where $\hat{V}$ is in dimensional units. In steady state, Eq. (1) determines the electric fields felt by the ions. With the usual definitions,

$$\eta\equiv e\hat{V}/k_BT_e, \quad \lambda_D^2\equiv\varepsilon_0k_BT_e/n_0e^2, \quad c_S^2\equiv k_BT_e/M, \tag{2}$$

where n_0 is the quasineutral plasma density in the main plasma, Eq. (1) can be written as

$$\frac{\varepsilon_0k_BT_e}{n_0e^2}\hat{\nabla}^2\eta=\lambda_D^2\hat{\nabla}^2\eta=\left(\frac{n_e}{n_0}-\frac{n_i}{n_0}\right). \tag{3}$$

If w is the scale length of the gradient $\hat{\nabla}$, and we define $\mathbf{r}\equiv\hat{\mathbf{r}}/w$, so that $\nabla^2=w^2\hat{\nabla}^2$, yielding

$$\nabla^2\eta=\frac{w^2}{\lambda_D^2}\left(\frac{n_e}{n_0}-\frac{n_i}{n_0}\right)\approx 0. \tag{4}$$

W/λ_D is extremely small, and here it is squared. Though $n_i\gg n_e$ in the trench, n_i/n_0 is still <1. Thus, as long as $W^2/\lambda_D^2\ll 1$, we need to only solve the dimensionless Laplace's equation

[a]Electronic mail: tsitsi@lanl.gov.
[b]Deceased.
[c]Electronic mail: ffchen@ee.ucla.edu.

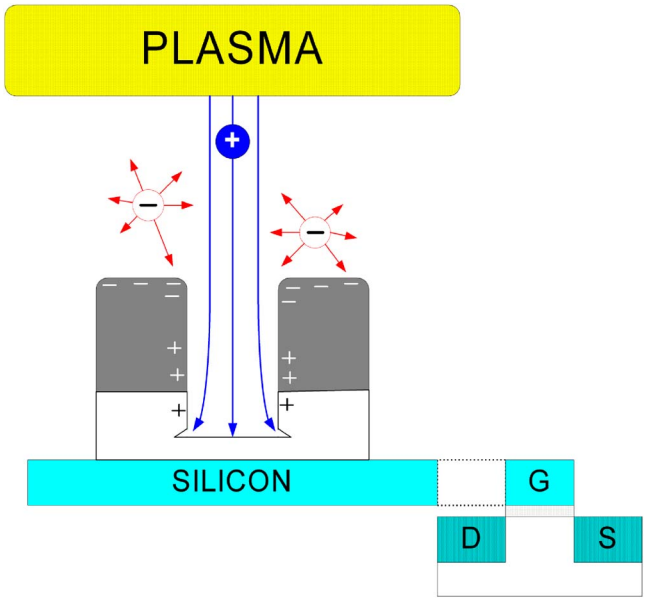

FIG. 1. (Color online) Geometry of plasma etching of a submicron feature. The dark material at the top is a patterned photoresist mask which defines the trench or via (hole) to be etched. The proximity of the plasma's sheath edge is greatly exaggerated.

$$\nabla^2 \eta = 0 \tag{5}$$

subject to the boundary conditions $\eta = \eta_b(\mathbf{r}_b)$ at $\mathbf{r} = \mathbf{r}_b$. The solution would be the same as that of the dimensional problem $\hat{\nabla}^2 \eta = 0$ with the boundary conditions $\eta = \eta_b(\hat{\mathbf{r}}_b)$ at $\hat{\mathbf{r}} = \hat{\mathbf{r}}_b$. Thus, only the aspect ratio of the trench matters, and not its absolute size, if the Debye length λ_D is $\gg w$. The space charge deep inside the sheath is negligible.

The ion trajectories are computed from

$$\frac{d^2\hat{\mathbf{r}}}{dt^2} = -\frac{e}{M}\hat{\nabla} V = -\frac{e}{M}\frac{k_B T_e}{e} \nabla \eta = -c_S^2 \hat{\nabla} \eta. \tag{6}$$

In terms of $\mathbf{r}$, this becomes $w^2 d^2\mathbf{r}/dt^2 = -c_S^2 \nabla \eta$. Defining $\tau \equiv c_S t/w$, we have

$$d^2\mathbf{r}/d\tau^2 = -\nabla \eta, \tag{7}$$

which has the same form as Eq. (6), regardless of w. Thus, the ion orbits are geometrically the same on any scale; only the time scale is changed. The computations are in these scale-independent dimensionless units. Collisions are completely negligible, since all mean free paths are longer than λ_D and hence much larger than s.

III. COMPUTATIONAL METHOD

The two-dimensional region used for computations is shown in Fig. 2. A block of dielectric with $\kappa \approx 4$ is surrounded by a vacuum sheath region bounded by a conductor representing the sheath edge, S dimensionless units away. In practice S is much larger than the feature size and its value is not significant. At the bottom of the trench, shown at the top in this inverted diagram, is a conducting "collector" representing the substrate being etched; the trench grows in the direction of increasing y. Ions are accelerated toward the dielectric block by the sheath electric field, and the surface

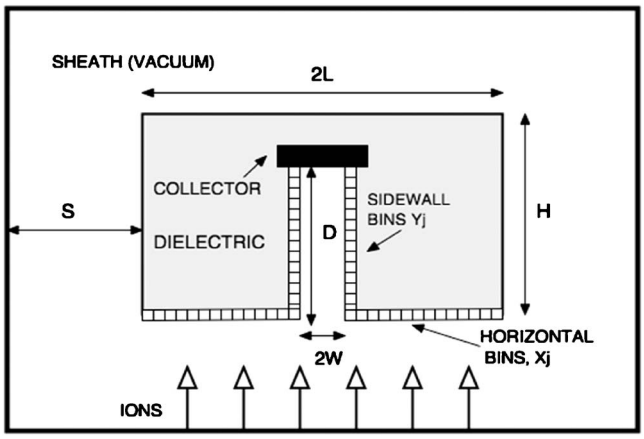

FIG. 2. Computational region. The sheath edge is at the bottom, and the trench is shown inverted, with the collector at the top. The outer region is vacuum, and the inner region a dielectric material. Ions are emitted from the sheath edge at the bottom.

they strike first is normally photoresist. The trench walls are photoresist near the entrance and either oxide or polymer-coated silicon further down. This geometry can represent either polysilicon etch with polymer deposition or oxide etch at the beginning of overetch. The photoresist surface is divided into cells x_j, while the trench walls are divided into smaller cells y_j. The dielectric has width $2L = 14$ and height $H = 10$, while the trench has width $2W$ and depth D, with aspect ratio $\mathrm{AR} = D/W$. Ions are injected vertically from the $V \equiv 0$ sheath edge at $y = 0$ with the Bohm velocity c_S. The collector is at an adjustable potential V_c.

We make three physically reasonable simplifying assumptions:

(1) The sheath edge is planar, and monoenergetic ions are ejected at 90° to it;
(2) The ion velocity at the sheath edge has the Bohm value c_S, corresponding to an energy $1/2 k_B T_e$;
(3) The electrons have a Maxwellian distribution everywhere. The last is true if V_c is negative, as is normal for a biased wafer, so that electrons see a repelling potential everywhere. The Boltzmann relation,

$$n_e/n_S = \exp[(V - V_S)/T_{\mathrm{eV}}], \quad T_{\mathrm{eV}} \equiv k_B T_e/e \tag{8}$$

then holds for any shape. Here $n_S = n_i = n_e$ at the sheath edge by definition, and we have taken V_S to be 0. Thus, the bulk plasma has potential $V = +1/2 T_{\mathrm{eV}}$.

The potential on a floating surface is found by equating the electron and ion fluxes. The electron flux is

$$\Gamma_e = n_e v_r = n_S v_r \exp[(V - V_S)/T_{\mathrm{eV}}], \tag{9}$$

where

$$v_r = \sqrt{(k_B T_e/2\pi m)}$$

is the random thermal velocity normal to a surface. The ion flux at $y = 0$ is simply

$$\Gamma_0 \equiv \Gamma_i(0) = n_S c_S = n_S \sqrt{(k_B T_e/M)}. \quad (10)$$

In the absence of a trench, the substrate surface charges to the usual floating potential V_f given by

$$(V_f - V_S)/T_{\mathrm{eV}} = -\ln\sqrt{(M/2\pi m)} \approx -4.68 \quad \text{for argon}. \quad (11)$$

We have set $V_S=0$, so that the computation is in a grounded box. Since V_S is $\approx -1/2T_{\mathrm{eV}}$ relative to the plasma, V_f is $\approx -5.18T_{\mathrm{eV}}$ relative to the plasma or ≈ -15 V for $k_B T_e=3$ eV in argon.

The potential to which each surface element Δx_j of the photoresist or Δy_j of the trench wall charges is computed as follows. Let N be the number of ions ($\approx 10^4$) emitted at $y=0$ over a surface area LZ per unit time, where Z is a length in the ignorable z direction. The emitted ion flux is $\Gamma_0 = N/LZ = n_S c_S$. If N_j ions strike a surface cell of width Δx_j, the ion flux to that cell is $\Gamma_{i,j} = N_j/\Delta x_j Z$. The ratio of this to the undisturbed flux Γ_0 is then

$$R(x_j) = (N_j/N)(L/\Delta x_j) = F(x_j)(L/\Delta x_j), \quad (12)$$

where $F(x_j)$ is the fraction of all ions that end up in cell x_j. The electron flux $\Gamma_{e,j}$ to a cell is $n_S v_r \exp(V_j/T_{\mathrm{eV}})$. Equating this to the ion flux $\Gamma_{i,j} = n_S c_S R(x_j)$, we have

$$v_r e^{V/T_{\mathrm{eV}}} = c_S F(x_j) L/\Delta x_j. \quad (13)$$

Using Eq. (11), we find the floating potential of that cell relative to the sheath edge to be

$$V(x_j) = T_{\mathrm{eV}}[\ln(F_j L/\Delta x_j) - 4.68], \quad (14)$$

where $F(x_j)$ is found by counting trajectories.

For a plasma characterized by $k_B T_e$ and ion charge-to-mass ratio, ion orbits are computed first with all insulating surfaces at potential V_f and the collector at potential V_c. A Poisson solver with a triangular grid[17] is used to calculate the 2D electric fields. The time-independent trajectory of each ion emitted from the sheath edge is then calculated with a C++ program written for this purpose. When the trajectory intersects a surface cell, its contribution to N_j is counted. The potential of each cell $V(x_j)$ is then calculated from Eq. (14) and used in the first iteration. The ion orbits are then recalculated, giving data for the next iteration. This is continued until N_j and $V(x_j)$ converge to steady values. When no ion falls on a cell, Eq. (14) diverges. In that case, we assume that the cell actually receives one ion or a fraction of an ion, resulting in $V(x_j) \approx -40$ V. The results are not sensitive to this approximation. In this model, we neglect all collisions, secondary emission, and surface currents, though a test of the last effect will be mentioned later. More details of this method are given in a dissertation.[18]

Because of the scale invariance of the problem, only two parameters need to be set for any given geometry: the aspect ratio AR and the collector potential V_c. For definiteness, all dielectrics are given a representative value of $\varepsilon_R=4$. Since the "time" steps are discrete, an ion trajectory does not necessarily intersect the boundary at the end of a step; the position has to be interpolated. The number of such stopping points in each cell provides the value of N_j described above.

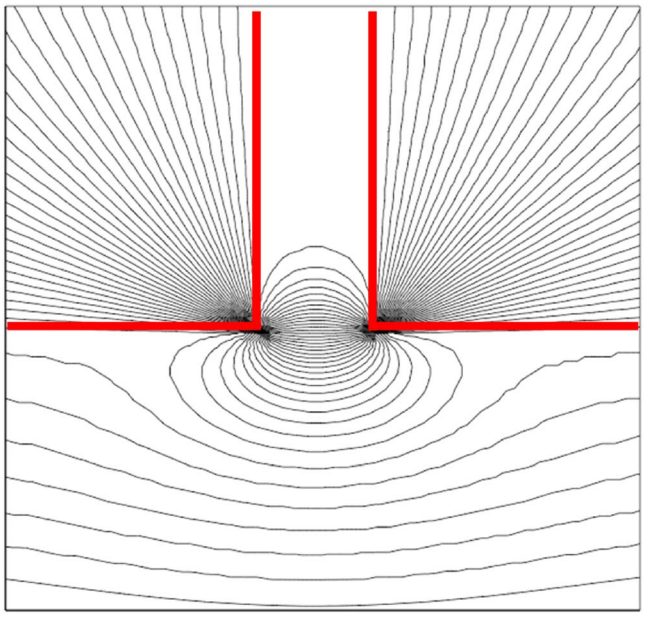

FIG. 3. (Color online) Equipotentials near a square trench entrance.

Once the iteration has converged, the orbits are universal curves for the given values of A_R, V_c, and $k_B T_e$. The density is irrelevant since, as shown above, the space charge is negligible. The size of the dielectric block does not matter as long as it is big enough.

IV. THE RESULTS

A. Ion shading

The E-field pattern near the trench entrance is shown in Fig. 3. Because of the sharp corners, the field is extremely strong there and causes a large deflection of the ions, as shown in Fig. 4(a). To suppress this unphysical effect, the corners were subsequently rounded into a circular arc. The resulting trajectories [Fig. 4(b)] are more reasonable, but the fact remains that no ions can strike the sidewall near the entrance. This ion shadowing effect, which occurs in addition to the well-known electron shading effect, is caused by

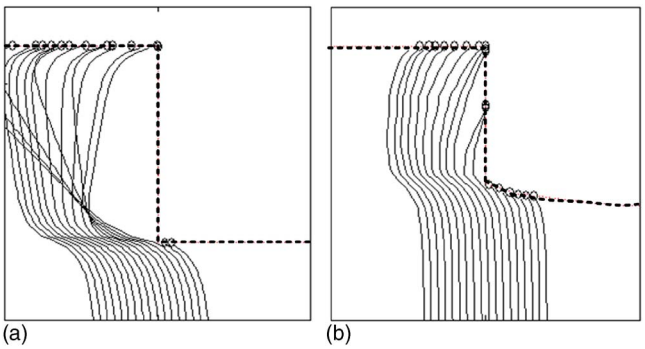

FIG. 4. (Color online) Ion orbits in a trench with (a) sharp edges and (b) rounded edges. The horizontal scale has been expanded to show the effect.

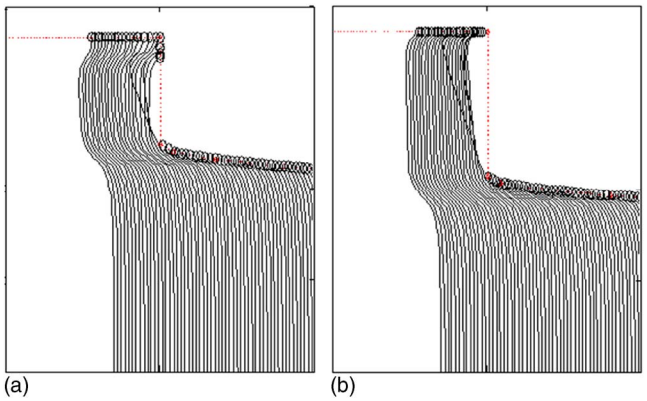

FIG. 5. (Color online) Ion shading effect for AR=5 and (a) V_c=26 V and (b) AR=7, V_c=40 V. The horizontal scale has been expanded.

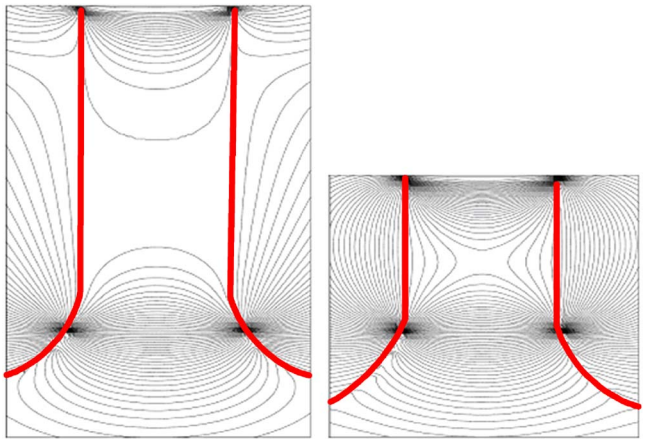

FIG. 8. (Color online) *E*-field patterns (equipotentials) for A_R=7 and 3, at V_c=−22 V.

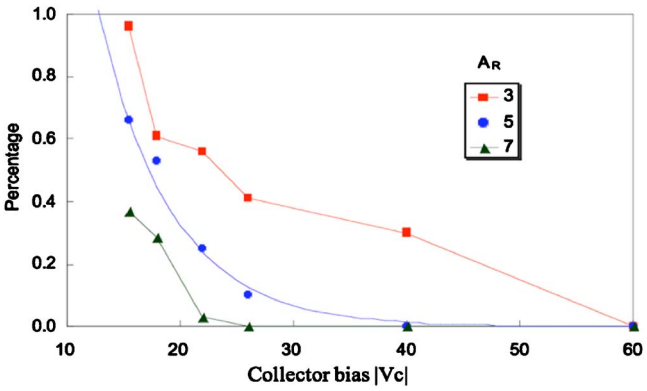

FIG. 6. (Color online) Percentage of emitted ions falling on the sidewalls as a function of collector bias $|V_c|$ for three values of A_R. The curve is an exponential fit to the A_R=5 data.

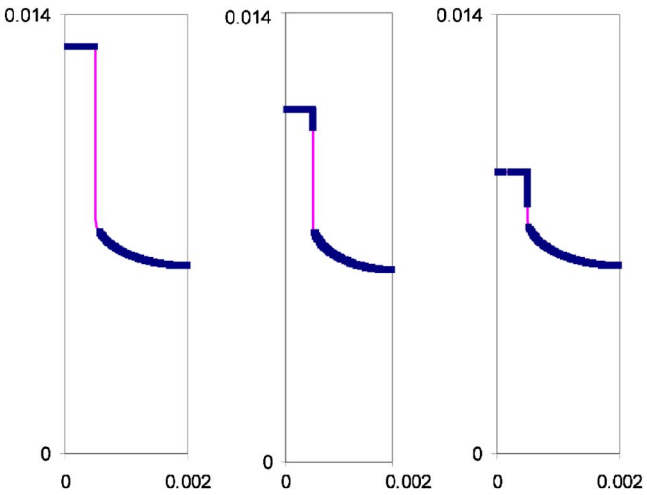

FIG. 7. (Color online) Ion collection regions in trenches with A_R=7, 5, and 3, with V_c=−26 V. The light regions of the trench wall are not struck by any ions.

the *E*-fields outside the trench, which curve the orbits inward. At large negative collector potentials, the entire sidewall can be protected from ion bombardment; this is shown in Fig. 5. The percentage of ions collected on the sidewall as a function of V_c is shown in Fig. 6 for three values of A_R. The decrease is more or less exponential. Physically, the ions gain enough energy at large $|V_c|$ that the negative sidewalls cannot deflect them. That the ion shading increases with A_R is a more subtle effect. Figure 7 shows the shaded regions for three values of A_R at constant V_c. The reason that ions are deflected into the sidewalls only for low A_R can be seen from the self-consistent field patterns in Fig. 8. It is seen that the fields are very strong at the ends of the trench, particularly at the corners. At A_R=7, the interior of the trench is essentially field-free. Ions are deflected into the sidewall only in the arc region. At A_R=3, the fields extend into the interior, where E_x is large enough to impart transverse momentum to the ions streaking in the *y* direction.

Ion shading also causes the collector current to saturate above a critical V_c above which no ions can be lost to the sidewalls. This is shown in Fig. 9.

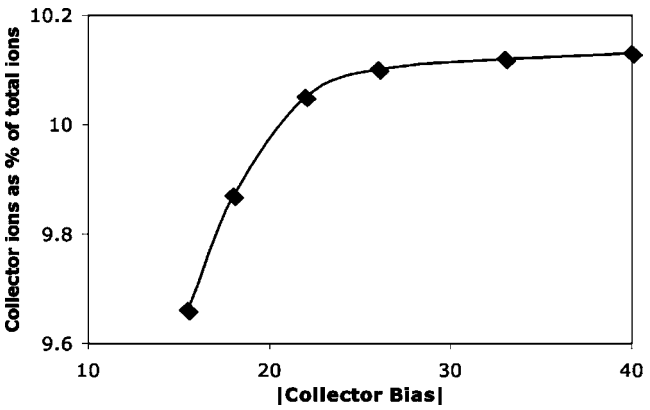

FIG. 9. Number of ions falling on the collector at A_R=7 as a function of collector voltage, expressed as a percentage of all ions emitted from x=−L to L.

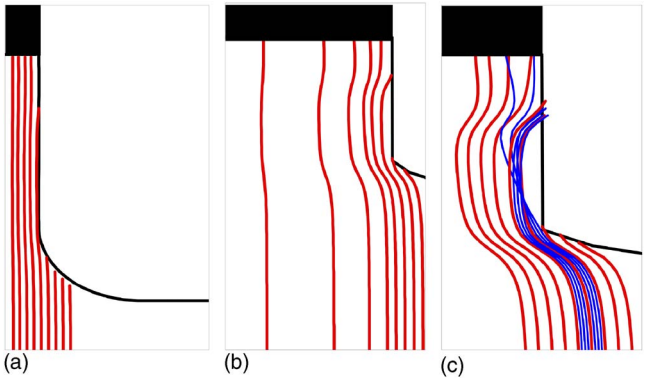

FIG. 10. (Color online) Ion orbits for $A_R=5$ and $|V_c|=26$ V with the horizontal scale (a) normal, (b) expanded by a factor 20, and (c) expanded by a factor 80 relative to the vertical scale. The orbit spacing has been decreased near the wall for clarity.

B. Nature of the ion trajectories

The quantitative results can be better understood if one first observes the nature of the ion orbits. Figure 10 shows three views of the trajectories at $A_R=7$ and $V_c=-26$ V. The ions enter the trench at high velocity, and their deflections are so small that they cannot be seen on this scale. In Fig. 10(b), the horizontal scale has been expanded by a factor 20. Here it can be seen that the ions enter the trench at an angle due to the external E-field. No ions strike the first part of the wall, which is shaded. The negative charges on the wall eventually deflect the ions outward, causing them to strike the corner of the trench. In Fig. 10(c), the horizontal scale has been stretched by a factor 80, and intermediate orbits have been plotted, shown by the thin lines. Orbits which pass near the corner of the photoresist actually cross and take shapes that are sensitive to the strong fields at the entrance corner. Note that the corner is actually circular but looks sharp only on this 80-to-1 scale. The pulling of ions into the trench by the charge on the photoresist is shown more clearly in Fig. 11. Incident ions (indicated by the solid lines) headed for the photoresist surface are drawn into the trench by the fields in the arc region. Since this region is charged negatively, the deflection direction is counterintuitive. However, the equipotentials shown in Fig. 8 show that the net E-field from all negative surfaces actually point away from the arc region.

The computations also showed that ions arrive at the collector with different energies. Most ions near the sidewalls are moving laterally and hit the sidewalls with less energy than those going straight into the collector, and therefore do not penetrate deeply.

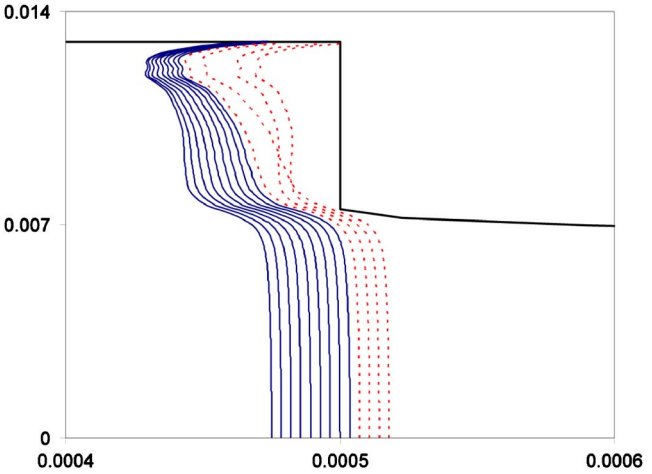

FIG. 11. (Color online) Ion orbits near the trench edge for $A_R=7$ and $V_c=22$.

TABLE I. Ion distribution with sharp and rounded trench entrances.

	Case A: Sharp corner	Case B: Sharp corner
	$A_R=7$, $V_c=-18$ V	
Collector	7.9%	9.9%
Sidewalls	0.5%	0.3%
Arc	N/A	20.7%
Flat surface	91.6%	69.1%
	$A_R=7$, $V_c=-26$ V	
Collector	8.2%	10.1%
Sidewalls	0.18%	0.00%

C. Effect of photoresist shape

Table I shows that fewer ions reach the collector if the corner is sharp rather than rounded. This is because the sharp corner more effectively shields ions approaching the trench at an angle. In either case, the fraction of ions hitting the sidewall is extremely small and cannot cause the trench profile defects that have been observed. As expected, the collector current increases and sidewall current decreases at the higher $|V_c|$ of 26 V. The difference between cases A and B is even more noticeable in the distribution of ions shown in Fig. 12. For the sharp entrance ions are collected over most of the sidewall, while for the rounded entrance, ions are shielded from all but the last few bins.

To see the effect of small changes in the entrance shape, we added a deformation in the form of a small bump onto the arc region in two locations. The statistics are shown in Table II for a sample of 50 000 ions. In case III, the bump is farther

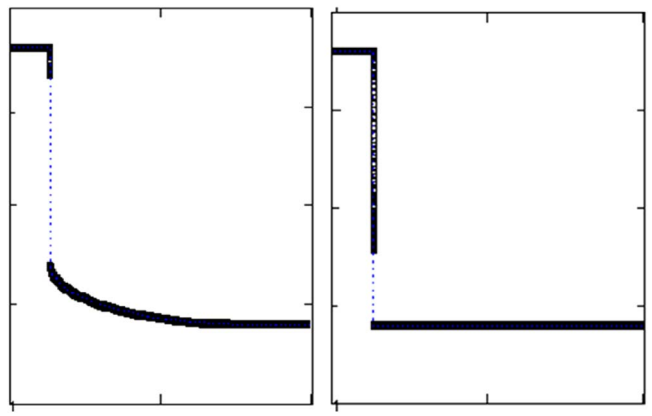

FIG. 12. (Color online) Distribution of ion collection for sharp and rounded trench entrances.

TABLE II. Ion distribution with small bumps.

	$A_R=7$, $V_c=-18$ V		
	Case I No bump	Case II Near bump	Case III Far bump
Collector	9.9%	8.6%	9.0%
Sidewalls	0.3%	0.0%	1.8%
Arc	20.7%	17.7%	17.4%
Flat surface	69.1%	73.7%	71.8%

from the trench than in case II (Fig. 13). The self-consistent equipotential lines for these three cases are shown in Fig. 14 and the ion sidewall distributions are shown in Fig. 15. The histograms show the number of ions that are collected in each of the 22 sidewall bins. In this case, bin number 1 corresponds to the trench entrance while bin 22 is at the collector. In case I, with a rounded entrance but no bumps, the E-field is very strong near the entrance. It is clear that even a small deformation of the photoresist will change the ion orbits drastically. The ions are given a kick at the entrance and then coast to the trench bottom through the nearly field-free trench. The collector is given only a small bias in this example, so that ions are not strongly drawn into it; some of them hit the sidewall near the bottom, giving rise to E-fields near the bottom corner.

In case II, the bump shadows part of the arc region, and the negative surface charge in the shadow gives the ions an extra kick, causing them all to land on the collector. In case III, the bump is far enough back that the ions are deflected into the arc region, lowering the field there. Having undergone less acceleration, the ions are drawn by transverse fields into the sidewall. Nonetheless, the top part of the sidewall is still shadowed. This sensitivity to the exact shape of the photoresist means that the ion orbits change during the etch and cannot be predicted. Fortunately, the ion flux to the sidewalls is in every case so small compared with that on the collector that it cannot significantly affect the quality of the etch.

D. Effect of overall geometry

The conducting surface connected to the trench bottom can extend beyond the trench, and this can affect the electric fields in the trench. To study this, we changed the collector shape. Figure 16 shows three collector geometries. In Fig. 16(a), the collector has the same width, $2W$, as the trench. In Fig. 16(b), the collector has a width of $4W$ or $8W$. In Fig. 16(c), the trench extends into a collector of width $4W$. This represents the case of polysilicon etch, the entire dielectric part being a photoresist.

1. Change of collector width

When the collector width is increased, the number of ions hitting the sidewall is shown in Table III for $A_R=5$, two values of V_c, and three collector widths, taken from a total sample of 26 515 ions. The distribution of ions on the sidewall in the $V_c=-26$ V case is shown in Fig. 17. Though the statistics are poor, the trend is that wider collectors allow more ions to the sidewalls. The reason is that the equipotential lines near the trench bottom are essentially straight for collector widths greater than $4W$, while for a width of $2W$ the lines are curved, and the corresponding E-field pulls ions away from the wall.

2. Etching into the metal

In the configuration of Fig. 16(c), we have examined the cases of $A_R=5$ and 7 and $V_c=-26$ V and -15.5 V, with two or six bins (out of 14) extending into the metal. This geometry studied is shown again in Fig. 18(a), and the field pattern in Fig. 18(b). Ion orbits near the wall are shown in Fig. 18(c), including the transition between dielectric and metal walls. From these computations, we observed that:

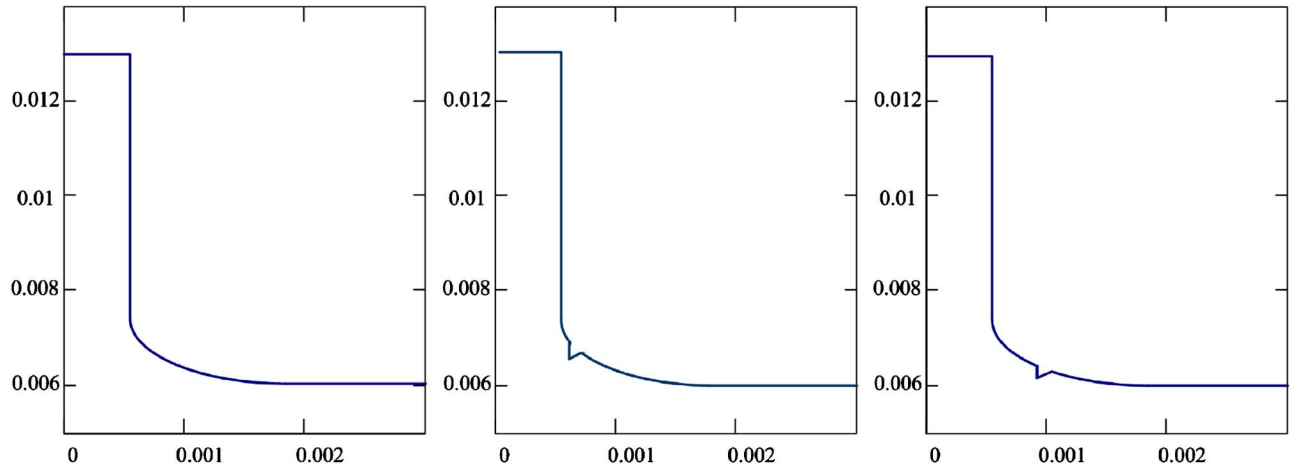

FIG. 13. (Color online) Profiles of trench entrances without and with bumps. From left to right in the figure we have case I (no bumps), case II (near bumps), and case III (far bumps) on the photoresist.

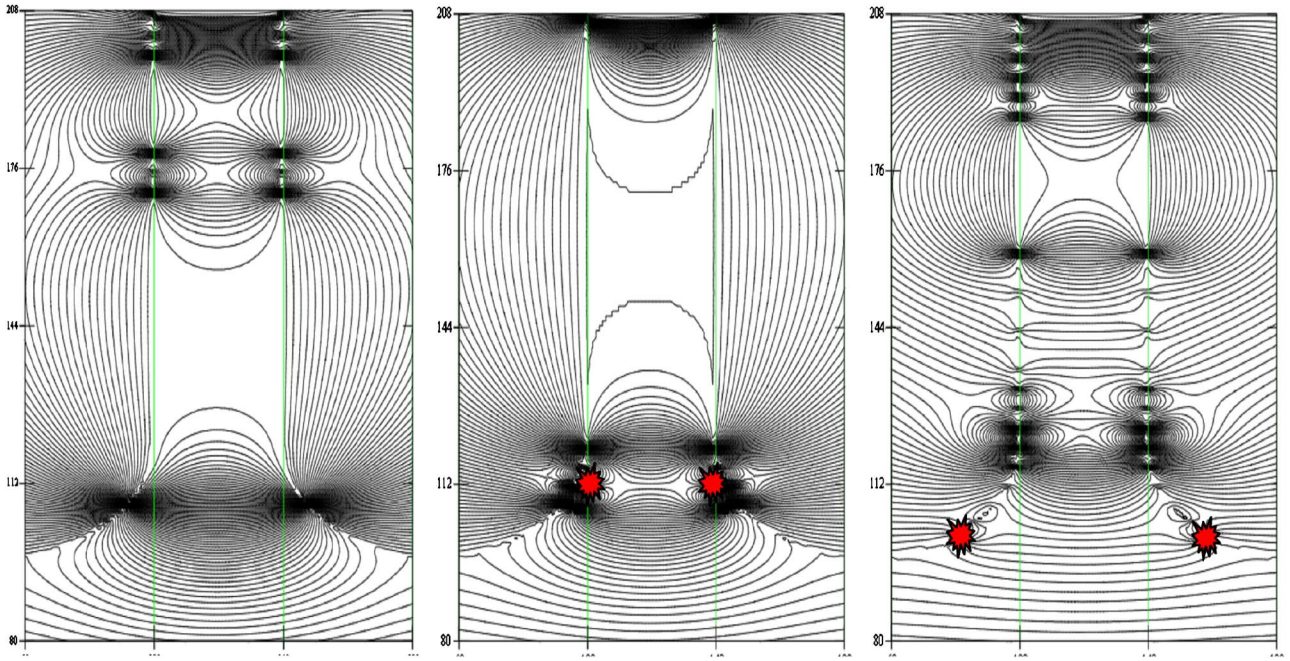

FIG. 14. (Color online) Field patterns for Fig. 13.

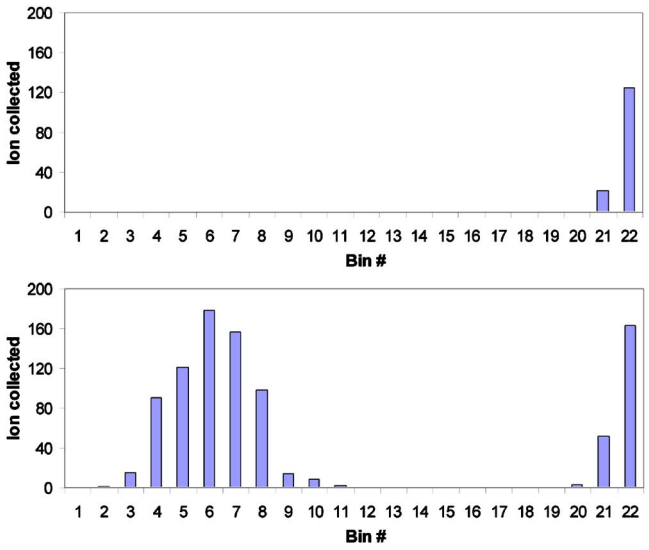

FIG. 15. (Color online) Sidewall ions location for cases B and D. No ions were collected on the sidewalls for C.

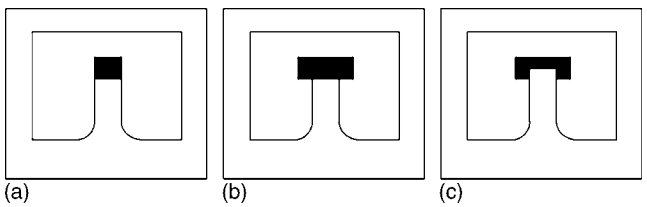

FIG. 16. Changes in collector shape.

TABLE III. Sidewall ions with wide collectors.

	$2W$	$4W$	$8W$
−18 V	141	154	157
−26 V	30	35	37

(a) at low $|V_c|$ ions landed in both the metal and the dielectric parts of the sidewall,
(b) deeper penetration into the metal results in fewer ions to the dielectric, and
(c) the same trends occur at $A_R=5$ as at $A_R=7$.

3. Multiple trenches

To see the effect of neighboring trenches, we considered a double trench configuration. Since both collectors are biased to the same potential, the ions in each trench are attracted by the field of the collector on the other trench. This results in an asymmetry, seen in the orbits of Fig. 19, such that more ions strike the inner sidewall than the outer one. The histogram in Fig. 20 shows the distribution of ions on the sidewalls and collector when a total of 25 000 ions were injected from the sheath edge in the computation. The insert gives only the collector distribution of ions and it shows that this is also slightly asymmetric. Compared with an isolated trench, there are more sidewall ions: 2.6% of 25 000 injected

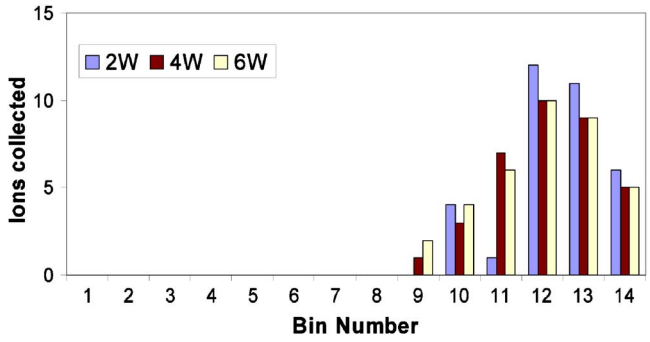

FIG. 17. (Color online) Distribution of sidewall ions for three collector widths. The entrance is at the left and the collector at the right.

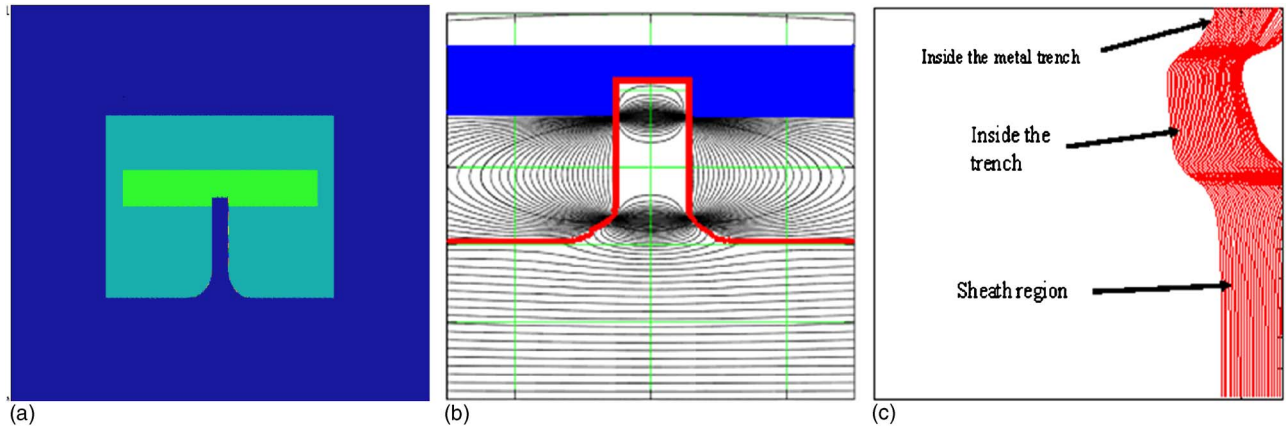

FIG. 18. (Color online) Computational region (a) and equipotential lines (b) for trenches extending into the metal. (c) Ion orbits near the wall for $A_R=5$ and $V_c=-15.5$ V.

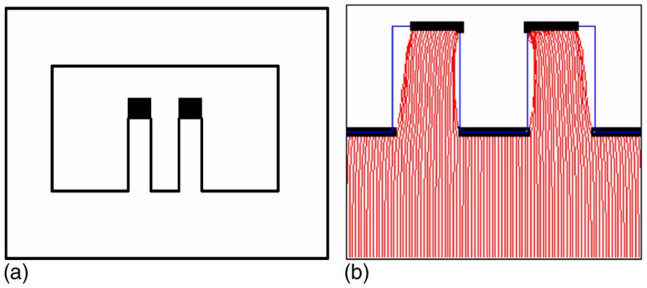

FIG. 19. (Color online) (a) A double-trench configuration. (b) Ion orbits in neighboring trenches, with $A_R=5$ and $V_c=-26$ V.

ions versus 0.5%, or an increase of 2.5% per trench. Even with this increase, the fraction of all ions entering a trench is still very small, and it decreases with increasing $|V_c|$.

4. Effect of dielectric constant

In these calculations, the dielectric constant κ, is assumed to have a value of 4 for all insulating materials. To see if a low-k material changes the results, we have compared $\kappa=4$ with the rather extreme value $\kappa=2$ and show results for the case $A_R=5$, $V_c=-24$ V in Fig. 21. The ions suffer small deflections at $\kappa=2$, resulting in a lower percentage of sidewall ions: 0.06% versus 0.11%. Since the numbers are so small, this difference does not affect our general conclusions.

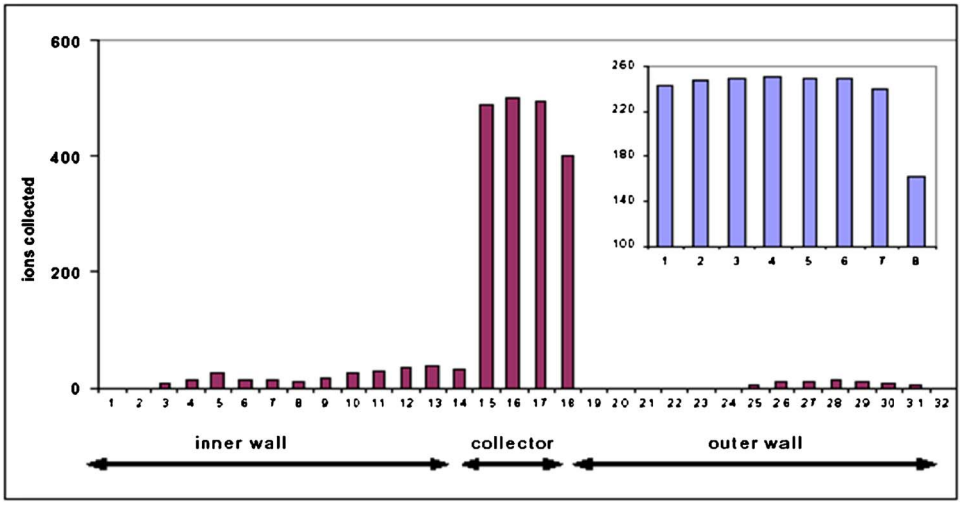

FIG. 20. (Color online) Distribution of ions collected on the inner and outer walls and on the collector of neighboring trenches. The inset is a detail of the distribution on the collector.

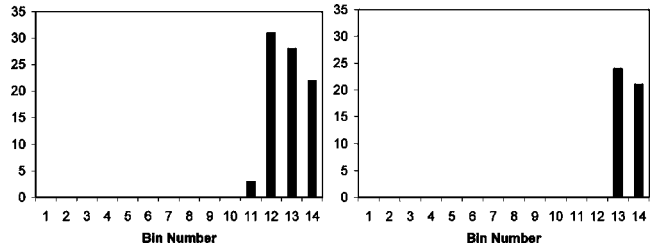

FIG. 21. Distribution of ions along the trench wall for $k=4$ (left) and $k=2$ (right). Bin number 1 is at the trench entrance and collector is at the right.

V. SUMMARY AND CONCLUSIONS

By reducing the problem to a simple dimensionless form, universal curves were obtained for ion trajectories in etched trenches, self-consistently with the sidewall potentials. If ion reflections from the walls are ignored, results depend on only two parameters: the aspect ratio A_R, and the potential V_c at the trench bottom. Principal findings are as follows:

(a) Electric fields external to the trench cause the ions to enter the trench at an angle. This causes an *ion shading* effect. This effect protects the top part of the trench, and sometimes all of it, from ion bombardment.
(b) Ion orbits are determined mainly by the strong fields at the corners of the entrance. From there they coast through the trench with little additional deflection.
(c) In spite of the strong fields at the entrance, ion orbits are nearly straight and vertical. So few ions strike the sidewall that they cannot cause deformations of the trench profile.
(d) The small ion flux to the walls is very sensitive to the exact shape of the photoresist at the top. This will change in an unpredictable way during the etching process.
(e) Contrary to intuition, a deep trench with large A_R will have no ions striking the wall.

These observations differ from commonly held conceptions of how the ion flux behaves in reactive ion etching. By examining the variation with A_R, one can get an idea of the changes in ion behavior as the etch progresses. By varying V_c, one can gauge the changes during an rf cycle.

ACKNOWLEDGMENTS

This work was supported by UC Discovery Grants, Applied Materials, Inc., and the National Science Foundation.

[1] M. A. Lieberman and A. J. Lichtenberg, *Principles of Plasma Discharges and Materials Processing* (Wiley, New York, 1994).
[2] G. S. Oehrlein, M. F. Doemling, B. E. E. Kastenmeier, P. J. Matsuo, N. R. Rueger, M. Schaepkens, and T. E. F. M. Standaert, IBM J. Res. Dev. **43**, 181 (1999).
[3] S. M. Sze, *Physics of Semiconductor Devices* (Wiley, New York, 1981).
[4] S. M. Rossnagel, J. J. Cuomo, and W. D. Westwood, *Handbook of Plasma Processing Technology: Fundamentals, Etching, Deposition, and Surface Interactions* (William Andrew Publishing/Noyes, New York, 1990).
[5] B. R. Rogers and T. S. Cale, Vacuum **65**, 267 (2002).
[6] G. S. Oehrlein, Surf. Sci. **386**, 222 (1997).
[7] F. F. Chen, *Plasma Physics and Controlled Fusion* (Plenum, New York, 1990).
[8] K. Hashimoto, Jpn. J. Appl. Phys., Part 1 **32**, 6109 (1993).
[9] K. Hashimoto, Jpn. J. Appl. Phys., Part 1 **33**, 6013 (1994).
[10] S. Sakamori, T. Maruyama, N. Fujiwara, H. Miyatake, and M. Yoneda, Jpn. J. Appl. Phys., Part 1 **36**, 2521 (1997).
[11] G. S. Hwang and K. P. Giapis, J. Vac. Sci. Technol. B **15**, 1839 (1997).
[12] S. Sakamori, T. Maruyama, N. Fujiwara, and H. Miyatake, Jpn. J. Appl. Phys., Part 1 **37**, 2321 (1998).
[13] M. Aoyama, T. Ito, M. Inoue, and Y. Shioya, Vacuum **51**, 555 (1998).
[14] K. P. Giapis and G. S. Hwang, Jpn. J. Appl. Phys., Part 1 **37**, 2281 (1998).
[15] T. Kamata and H. Arimoto, J. Vac. Sci. Technol. B **14**, 3688 (1996).
[16] T. Kamata and H. Arimoto, J. Appl. Phys. **80**, 2637 (1996).
[17] TriComp E-Stat 6.0, and TriComp Mesh 6.0 Codes, Copyright Field Precision [Online]. Available: http://www.fieldp.com
[18] T. G. Madziwa-Nussinov, Ph.D. thesis, UCLA (2003).